Draft version August 21, 2026
Typeset using LaTeX **twocolumn** style in AASTeX7.0.2

Salt Diapirism in Europa's Periodically Thickening Icy Shell

Mariam Helal[1] and Elvira Mulyukova[2]

[1] *Univeristy of California, Berkeley, Department of Astronomy and Department of Earth & Planetary Sciences*
[2] *Northwestern University, Department of Earth, Environmental, and Planetary Sciences*

ABSTRACT

The solid outer shell of icy satellites is the primary barrier to transporting heat and chemical species from their interiors to their surfaces. The overturn of Europa's ice shell is driven by tidal heating and spatial variations in dense ice impurities such as salt. The rate of tidal heating varies periodically with time due to orbital variations in eccentricity, driving subsequent changes in the thickness of the ice shell. During periods of thickening, a new basal ice layer forms out of Europa's salty ocean with lower salt concentrations than the overlying older ice. The positive buoyancy of this basal layer drives the formation of salt diapirs, providing an additional mechanism for Europa's ice overturn. The contribution of salt diapirism to the overall transport of material in the ice shell is influenced by the shell growth rate at the ice-ocean interface, which in turn impacts the rheological properties and salt content of the ice. In particular, a faster growing basal layer yields higher salt concentrations and finer grain sizes, producing a smaller compositionally induced density contrast and a mechanically weaker layer. We apply a Rayleigh–Taylor instability framework to calculate the spacing, size, and ascent velocity of salt diapirs across a range of plausible Europan physical parameters. These predictions can be compared with observations of surface features potentially of diapiric origin to evaluate whether salt diapirism is capable of transporting material from Europa's interior to the surface over geologically relevant timescales.

Keywords: Europa (2189) — Jovian satellites (872) — Thermal properties (Ice) (2278) — Planetary science (1255) — Planetary geology (2288) — Geological processes (2289)

1. EUROPA AS AN ICY SATELLITE

Europa is an icy satellite of Jupiter characterized by a global, salty, subsurface ocean and icy shell, as seen in Figure 1. Surface observations of Europa suggest its ice shell may undergo solid-state convection, potentially transporting material from the interior towards the surface (W. B. McKinnon 1999).

Several different mechanisms may contribute to this overturn of ice. One such driver is the vertical thermal contrast present in the shell due to internal heating provided by the satellite being tidally flexed by Jupiter (G. Tobie et al. 2003). However, previous work has shown that this alone is not enough to produce observed dome and spot-like surface features which are thought to be the result of material upwelling in the ice shell (R. T. Pappalardo & A. C. Barr 2004). An additional driver is necessary, one of which could be salt diapirism. Europa undergoes orbital cycles that induce changes in its eccentricity and therefore the amount of tidal dissipation in its interior H. Hussmann & T. Spohn (2004). This causes the periodic thickening and thinning of its ice shell. During periods of thickening, new ice is frozen out of the ocean. This basal ice is cleaner of impurities

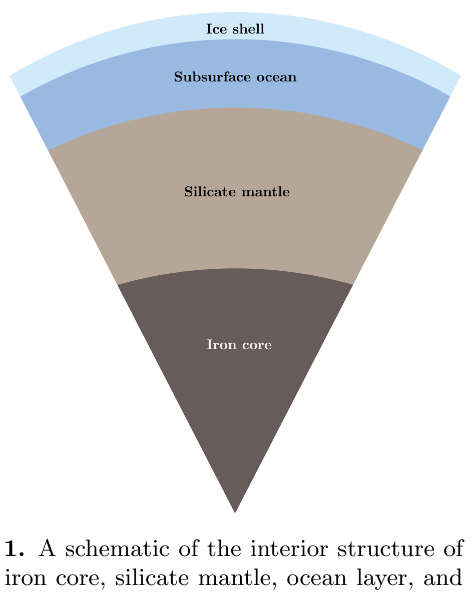

Figure 1. A schematic of the interior structure of Europa, with an iron core, silicate mantle, ocean layer, and ice shell (J. H. Roberts et al. 2023)

then the older overlying ice shell therefore more buoyant, driving the upwelling of salt diapirs (J. J. Buffo et al. 2020). Additionally, existing impurities melt and drain under the lower pressures experienced by the diapir as it rises, providing further upwelling force (R. T. Pappalardo & A. C. Barr 2004). However, the extent of the contribution of salt diapirism to material transfer Europa's ice shell is not fully understood. The goal of this project is to quantify this contribution by coupling the continuum scale model of density-driven flow and microphysical creep models of crystalline materials (such as ice, in the context of Europa's outer shell). We explore the scenario in which the ice shell is thickening, under the assumption that the rate at which the ice shell thickens impacts the rheology of the ice as well as the salt concentration of the resulting "cleaner" basal ice layer. For faster ice growth rates, ice grains being crystallized out are smaller (Y. Ren et al. 2024a), leading to smaller viscosities due to grain size sensitive ice deformation mechanisms (A. C. Barr & W. B. McKinnon 2007), and more salt is entrained (J. J. Buffo et al. 2020). In the case of slow ice growth, on the other hand, ice grains are larger, viscosities are higher, and salt concentrations are lower. We hypothesize that the impact of differences on ice growth rate on the physical properties of the basal ice layer will have cascading effects on the types of diapirs produced, illustrated in Figure 2.

We aim to determine the spacing of diapirs produced from the basal layer, as well as the timescale of their rise, within the context of these two end-member scenarios as well as in different coupling regimes. This timescale and the effect of parameter coupling on it can then be used to clarify the role of salt diapirism in producing surface features, such as domes, that are thought to be of diapiric origin (R. T. Pappalardo et al. 1998) (F. Nimmo & M. Manga 2009). Additionally, consideration of diapirs across Europa's surface will be used to determine the material and salt flux from the ocean to the surface and the global cycling time.

2. APPLICATION OF RAYLEIGH–TAYLOR INSTABILITY AND STOKES VELOCITY FOR DETERMINING DIAPIR ASCENT TIME

To quantitatively determine the spacing of diapir formation, we apply the Rayleigh–Taylor instability setup. This framework, discussed in J. A. Whitehead Jr. & D. S. Luther (1975) and originally formulated by S. Chandrasekhar (1961), describes a fluid layer overlaying less dense, buoyant material. Gravitational instability is produced when some perturbation, of a certain wavelength λ, occurs in the interface between these layers. This perturbation causes a difference in pressure

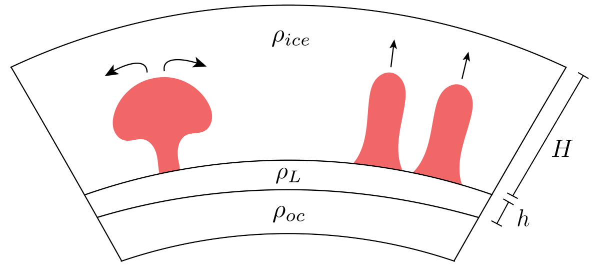

Figure 2. A schematic of the model set-up. A solid basal layer of ice freshly frozen out of the liquid ocean with a density of $\rho_{\rm oc}$. The basal layer has thickness h and density ρ_L, and is overlaid by ice of thickness H and density $\rho_{\rm ice}$. Diapirs rise out of the basal layer, forming into different possible shapes.

that drives fluid flow. Using conservation of mass and assuming the fluid is incompressible, the velocity function of the fluid flow can be determined, which is then used to derive a characteristic growth time (Equation 1) of the upwellings that will grow out of the basal layer based on the wavenumber that represents their spacing.

$$\tau = \frac{K\mu_L}{g\Delta\rho h}\,\frac{S + K + 2\frac{\mu_{\rm ice}}{\mu_L}C + \frac{\mu_{\rm ice}}{\mu_L}^2(S-K)}{C - 1 + \frac{\mu_{\rm ice}}{\mu_L}(S-K)}. \tag{1}$$

$$\Delta\rho = \rho_{\rm ice} - \rho_L \tag{2}$$

$$K = 2kh \tag{3}$$

$$k = \pi/\lambda \tag{4}$$

$$C = \cosh(K) \tag{5}$$

$$S = \sinh(K) \tag{6}$$

g is the gravitational acceleration; $\mu_{\rm ice}$ and $\rho_{\rm ice}$ are the viscosity and density of the overlying ice shell, respectively; and μ_L, ρ_L, and h are the viscosity, density, and thickness of the basal layer, respectively. The growth time is a function of K, the dimensionless wavenumber. The dominant wavenumber of the perturbation out of which diapirs grow is the one that minimizes the growth time, illustrated in Figure 3.

Using Rayleigh–Taylor instability, we determine the dominant spacing of the diapirs that will be produced out of the basal fresh ice layer. The diapir spacing can then be used to ascertain the total number of diapirs, modeled as upwelling spheres (see Figure 4), for a given surface area, as well as their radii. These values are then used to determine the Hadamard–Rybczynski Stokes velocity of the diapirs (Equation 7).

$$v = \frac{2\Delta\rho g R_D^2}{3\mu_{\rm ice}}\left(\frac{\mu_{\rm ice} + \mu_L}{2\mu_{\rm ice} + 3\mu_L}\right) \tag{7}$$

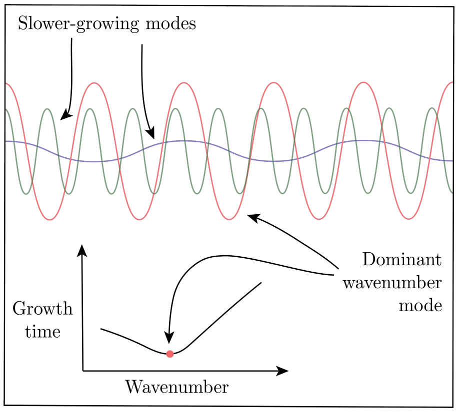

Figure 3. An illustration of how the dominant wavenumber of diapir spacing is determined, based on the wavenumber that minimizes the upwelling growth time.

v is the terminal rise velocity of the diapir, and R_D is the diapir radius. This rise velocity is used to determine the total time it takes the diapir to traverse the thickness of the ice shell, H.

$$t_{\text{rise}} = H/v \tag{8}$$

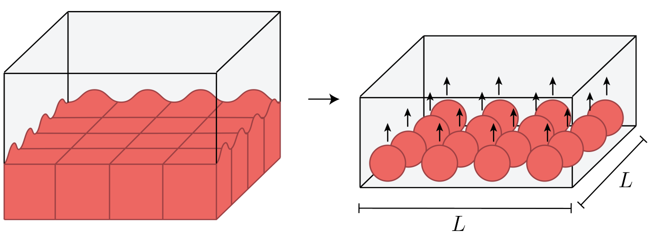

Figure 4. An illustration showing the start of the modeled spherical diapirs from the original dominant perturbation of the interface between the basal layer and ice shell. Our model considers a region characterized by $L = 100$ km to determine the volume and radius of each diapir, as well as the total number of diapirs within the region of interest.

The three main uncertain physical parameters governing the characteristic timescale τ and Stokes velocity v and therefore ascent time of the diapirs are: the ice shell and basal layer thickness, the viscosity of both layers, and the density contrast between them. The exact values of these parameters on Europa are not known. However, many previous studies have used thermal and chemical models of Europa's interior, as well as empirical studies of ice rheology, to provide estimates of the values themselves as well as other properties used to determine them, such as stress, ice grain size, salt concentrations, ice growth rates, and temperature. These values, as well as set model parameter values, can be found in Table 1. Additionally, a summary of default model parameter values used when not exploring how results vary during parameter sweeps can be found in Table 2. Our project introduced novelty in the coupling of ice growth rates to ice thickness, viscosity, and the density contrast, explained in the following sections.

2.1. *Ice Shell Thickness in Response to Tidal Variations*

The thickness of Europa's ice shell, H, as well as of the basal layer, h, are critical parameters in controlling the extent of diapir formation and rise through Equations 1 and 8. In the Rayleigh–Taylor framework considered here, h is a key input in determining the dominant spacing of the diapirs. Furthermore, H directly affects the rise timescale of diapirs by controlling the distance diapirs must traverse in order to reach the surface of the ice shell,

The total thickness of Europa's ice shell is controlled by heat transfer and tidal dissipation within the ice shell, which are themselves dependent on viscosity and the vertical density profile of the shell. The temporal variations in Europa's orbital eccentricity which induce changes in ice shell thickness occur at regularly timed intervals of period P_{growth}, determined through thermal-orbital evolution models of Europa.(H. Hussmann & T. Spohn 2004). This period, along with the ice growth rate (dh/dt), is used to determine h.

$$h = \frac{dh}{dt} P_{\text{growth}} \tag{9}$$

In this work, we consider a range of possible shell thicknesses and ice growth rates, alongside their impact on grain size and salt entrainment.

2.2. *Ice Deformation and Viscosity*

Viscosity is a measure of a material's resistance to deformation under an applied stress. In the context of Europa's ice shell, the ice undergoes solid-state creep over long timescales due to this stress. Viscous flow can be quantified with the following equation:

$$\dot{\epsilon} = \frac{\sigma}{2\mu} \tag{10}$$

where σ is the applied shear stress, $\dot{\epsilon}$ is the resulting strain rate, and μ is the material viscosity.

Ice deformation can occur through several deformation mechanisms, including diffusion creep, dislocation creep, grain boundary sliding, and basal slip. Diffusion creep, which involves the movement of vacancies (atoms missing within the crystal lattice), and grain boundary sliding, which involves ice grains sliding along their boundaries, are grain size sensitive mechanisms that are more important at relatively low stresses and fine grain sizes. Dislocation creep, which occurs due to the movement of dislocations (a linear defect in the crystal lattice), and basal slip, which involves dislocations moving along preferential planes for slip, are largely grain size insensitive and dominate at higher stresses. The relative contribution of each mechanism depends on temperature, stress, and grain size (W. B. Durham et al. 2010). In grain size sensitive regimes, smaller grains generally result in weaker ice with lower viscosities. In this study, each of these deformation mechanisms is considered in determining the total effective viscosity of the ice shell and basal layer.

For dislocation creep, grain boundary sliding, and basal slip, the effective viscosity is written as:

$$\mu_i = \frac{R^{m_i}}{2A_i}\sigma^{1-n_i}\exp\left(\frac{E_i}{R_G T}\right) \tag{11}$$

where μ_i is the effective viscosity of deformation mechanism i, A_i is the flow-law prefactor, E_i is the activation energy, n_i is the stress exponent, m_i is the grain size exponent, R is the grain size, σ is the applied shear stress, R_G is the gas constant, and T is temperature. Each mechanism has its own value for m_i based on its dependence on grain size. We assume ice is isotropic and that regardless of the direction of applied stress, the effect on its strength will remain the same, allowing for the usage of σ (the second invariant of the stress tensor) rather than the stress tensor itself.

In the case of diffusion creep, the effective viscosity is determined by the following equation:

$$\mu_{\text{diff}} = \frac{1}{2}\left(\frac{3R_G T_b R^2}{42 V_m D_{\text{diff}}}\right)\exp\left(\frac{E_{\text{diff}}}{R_G T}\right) \tag{12}$$

where T_b is the basal ice shell temperature, V_m is the molar volume of ice, D_{diff} is the volume diffusion coefficient, and E_{diff} is the activation energy for diffusion creep.

The total composite viscosity is obtained by combining the individual mechanisms through the following equation, assuming that the mechanism which accoomodates stress most readily will dominate:

$$\mu_{tot} = \left(\frac{1}{\mu_{\text{diff}}} + \frac{1}{\mu_{\text{disl}}} + \frac{1}{\mu_{\text{gb}} + \mu_{\text{bs}}}\right)^{-1} \tag{13}$$

The impact of grain size, stress, and temperature on the total effective viscosity of ice can be seen in Figure 5.

Viscosity is also strongly influenced by impurities, which can impact grain size and the individual deformation mechanisms. The relationship between impurity concentration and strength, however, is complicated. Impurities can alter grain boundary migration and recrystallization, though the exact impact is also dependent on where impurities are located (N. Stoll et al. 2021). Therefore, a lower salt concentration does not necessarily correspond to stronger ice or vice-versa. Additionally, impurities are thought to reduce grain size, which is important control on the rheology of ice, as stated previously. In our model, we consider the impact of salt impurities in terms of grain boundary pinning as a cap on grain size (N. Stoll et al. 2021).

The rate of ice shell growth influences both impurity concentrations and grain size. Rapid freezing of the subshell ocean produces smaller ice grains in the fresh ice and can result in greater salt entrainment, while slower growth allows grains to form larger crystals and a greater ability for the ice to reject impurities like salts. Because grain size impacts the dominant deformation mechanism, the rate of ice formation can control the strength and viscosity of the newly formed basal ice layer. This coupling between ice growth rate, grain size, impurity concentration, and rheology is therefore critical for understanding salt diapirism in Europa's ice shell.

Additionally, the viscosity contrast between the basal layer and overlying ice shell determines the shape of produced diapirs. If the diapir material has a larger viscosity, its shape will be "finger-like". Alternatively, if the diapir material has a smaller viscosity, its shape will be more "mushroom-like." These shapes are illustrated in Figure 2. This viscosity contrast is also related to the spacing of the diapirs: "mushroom-like" diapirs have larger spacing between them when compared to "finger-like' diapirs.

2.3. *Density Contrast Due to Salt Entrainment Differences*

The density contrast between the basal ice layer and the surrounding ice shell produces the buoyancy driving diapir formation. In the Rayleigh–Taylor framework, the density contrast is defined as the difference between the surrounding ice and the basal layer, as seen in Equation 2. A larger positive density contrast results in a stronger buoyancy force and faster diapir ascent. We consider the scenario where this density contrast is produced by salt content differences. Specifically, the density of each layer is determine using a linear-mixing model.

$$\rho = \left(1 - \frac{C}{1000}\right)\rho_{\text{pure}} + \frac{C}{1000}\rho_{\text{salt}} \tag{14}$$

C is the concentration of salt, ρ_{pure} is the density of pure ice, and ρ_{salt} is the density of the salt impurity.

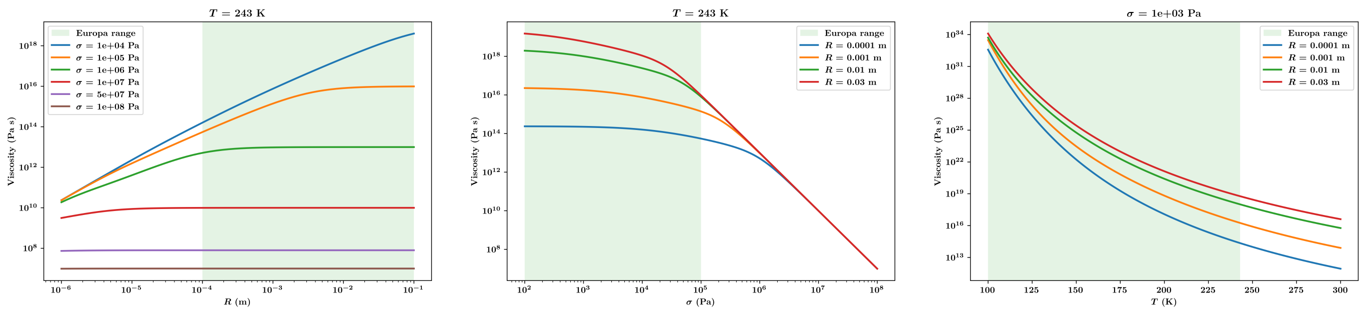

Figure 5. Comparisons of modeled viscosity against grain size, stress, and temperature, highlighting the range of physical parameters relevant to Europa's ice shell.

The magnitude of $\Delta\rho$ is strongly dependent on the rate of ice shell growth, which controls the ability of newly formed ice to reject ocean-derived impurities. Rapid ice growth limits the time available for salts to be rejected from the freezing ice. This results in greater salt entrainment within the newly formed basal ice layer (J. J. Buffo et al. 2020), producing a smaller density contrast. Therefore, rapidly formed ice is expected to have a lower $\Delta\rho$ and weaker compositional buoyancy. Conversely, slower ice growth allows for more efficient rejection of salts from the freezing front, producing cleaner ice. This creates a larger density difference between the basal layer and the surrounding shell, increasing the buoyancy available to drive diapirism.

3. RESULTS: PARAMETER COUPLING IMPACTS DIAPIR RISE TIME

Solving the coupled system of equations that comprise the model outputs the dominant spacing, size, and rise timescale of diapirs produced from the basal ice layer. This can be done across the range of plausible physical parameters described in Section 2. We explore the impact on variations in these physical parameters, described in Table 2, within Europan ranges as well as coupling between them in order to constrain the extent of salt diapirism in Europa's ice shell and its relationship with observed surface features. This can be done through an estimation of diapir-derived mass flux in the ice shell as well as comparisons between predictions of diapir size to observed dome sizes.

In order to create a baseline of the model behavior, a reference version of the model was run with all parameter values kept constant except for h (corresponding to specific ice growth rates for a fixed period of ice growth) and H, as seen in Figure 6. The results are as expected based on Equations 1, 8, and 7.

In order to determine how the ice growth coupling relationships described in Section 2 impact the results of the model and deviates from the reference, the coupling relationships were introduced one-by-one. First, the density coupling relationship was introduced, increasing ρ_L linearly with h based on defined minimum and maximum values for both parameters.

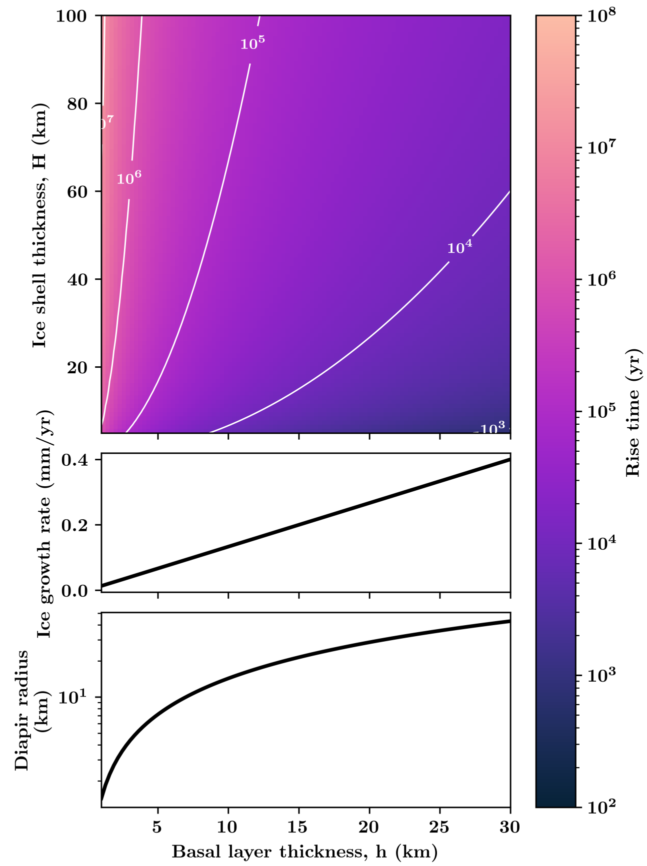

Figure 6. A reference heatmap illustrating how h and H impact $t_{\rm rise}$, with all other parameters kept constant according to values in Table 2. As expected, a larger H means it takes longer for the diapir to traverse the shell, according to Equation 8. A larger h produces a larger diapir, which increases the Stokes velocity according to Equation 7, therefore decreasing $t_{\rm rise}$. The bottom plot shows how ice growth rate varies with h for a fixed $P_{\rm growth}$.

$$\rho_L = (2.068965517 \times 10^{-4})h + 916.7931034 \qquad (15)$$

The results of this coupling is illustrated in Figure 7. In the reference case, increasing h leads to an continuous

Table 1. Estimated ice shell and ocean parameters

Parameter	Definition	Range / Value	Citation
		5×10^{13}	1
μ_{ice} (Pa s)	Viscosity of the ice shell	$10^{13} - 10^{15}$	2
		$10^{13} - 10^{15}$	3
		$3 - 60$	1
H (km)	Ice shell thickness	$20 - 45$	2
		$0 - 15$	4
		< 100	5
		$4.84 - 7.38 \times 10^{-12}$	1
dh/dt (m s^{-1})	Ice shell growth rate	$1.45 - 3.17 \times 10^{-12}$	2
		$2.5 \times 10^{-11} - 1.9 \times 10^{-10}$	3
C_{ice} (ppt)	Ice shell salt concentration	$1.053 - 14.72$	6
		$(0.001 - 0.1)C_{\mathrm{oc}}$	7
C_{oc} (ppt)	Ocean salt concentration	$1.1 - 88.3$	4
ρ_{oc} (kg m^{-3})	Ocean density	> 1200	5
R_{ice} (mm)	Ice grain size	$0.1 - 30$	8
T_b (K)	Basal temperature	243	9
σ (Pa)	Shear stress	$10^2 - 10^5$	10
T_s (K)	Surface temperature	100	1
g (m s^{-2})	Surface gravitational acceleration	1.31	2
P_{growth} (Ma)	Timescale of ice shell growth	75	1
ρ_{pure} (kg m^{-3})	Density of pure ice	917	11
E_{disl} (J mol^{-1})	Activation energy for dislocation creep	60000	8
E_{diff} (J mol^{-1})	Activation energy for diffusion creep	59400	8
E_{gbs} (J mol^{-1})	Activation energy for grain boundary sliding	49000	8
E_{bs} (J mol^{-1})	Activation energy for basal slip	60000	8
A_{disl} (Pa^{-4} s^{-1})	Pre-exponential factor for dislocation creep	4×10^{-19}	8
A_{gbs} (Pa$^{-1.8}$ m$^{1.4}$ s^{-1})	Pre-exponential factor for grain boundary sliding	6.2×10^{-14}	8
A_{bs} (Pa$^{-2.4}$ s^{-1})	Pre-exponential factor for basal slip	2.2×10^{-7}	8
n_{disl}	Stress exponent for dislocation creep	4	8
n_{gbs}	Stress exponent for grain boundary sliding	1.8	8
n_{bs}	Stress exponent for basal slip	2.4	8
m_{disl}	Grain size exponent for dislocation creep	0	8
m_{gbs}	Grain size exponent for grain boundary sliding	1.4	8
m_{bs}	Grain size exponent for basal slip	0	8
D_{diff} (m^2 s^{-1})	Volume diffusion coefficient	9.1×10^{-4}	8
V_m (m^3 mol^{-1})	Molar volume of ice	1.97×10^{-5}	8
R_G (J mol^{-1} K^{-1})	Universal gas constant	8.314	8

[a] References: (1) H. Hussmann & T. Spohn (2004); (2) J.-C. Chen et al. (2026); (3) G. Mitri & A. P. Showman (2005); (4) K. P. Hand & C. F. Chyba (2007); (5) S. D. Vance et al. (2018); (6) J. J. Buffo et al. (2020); (7) N. S. Wolfenbarger et al. (2022); (8) A. C. Barr & D. E. Stillman (2011); (9) F. Deschamps & C. Sotin (2001); (10) A. C. Barr & R. T. Pappalardo (2005); (11) J. J. Buffo et al. (2021).

increase in diapir size and therefore buoyancy, which decreases the growth time. However, introducing the coupling with ρ_L opposes this effect by reducing the density contrast for larger diapirs and therefore reducing the buoyancy. Eventually, the reduction in buoyancy by the density contrast wins out and the trend in rise time decrease reverses, until diapirism eventually stops once the density contrast is no longer positive.

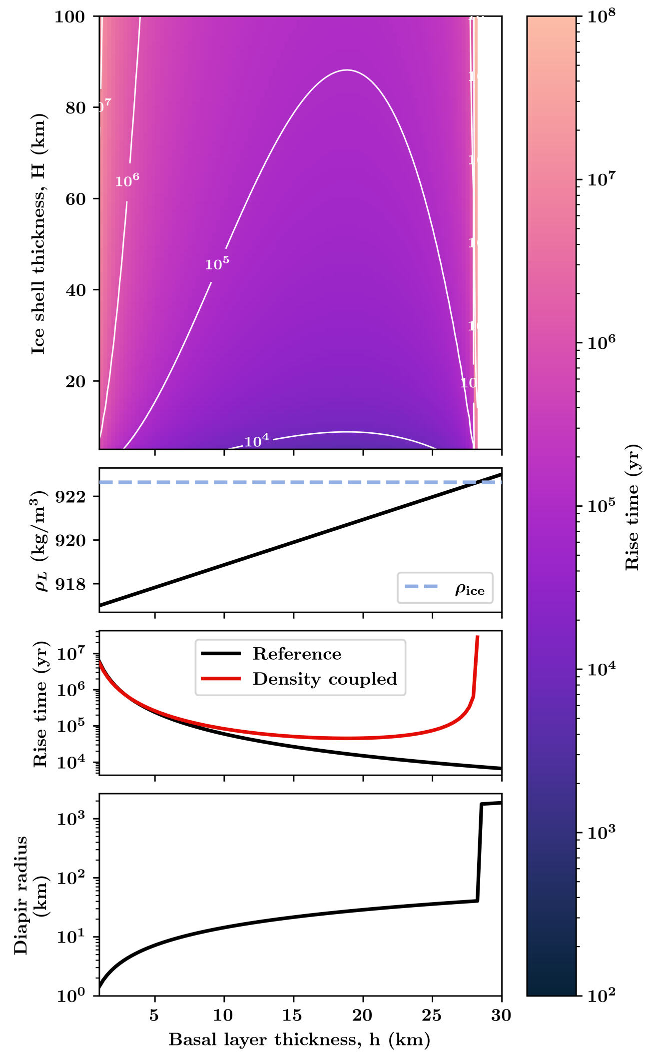

Figure 7. We introduce a coupling between ρ_L and h (Equation 15), where ρ_L increases with h. Because $\Delta\rho$ does not impact the dominant wavelength, the observed deviation from the reference is due to the dependence of v on $\Delta\rho$ (Equation 7). This coupling works to dampen the effect of h alone on the $t_{\rm rise}$. A discontinuity is seen when $\rho_L = \rho_{\rm ice}$ due to $\Delta\rho$ no longer being positive, stopping diapirism.

Next, an additional coupling between h and R_L is introduced, the results of which can be seen in Figure 8.

$$R_L = 10^(-1.379310345 \times 10^{-4})h - 1.862068966 \quad (16)$$

This new coupling works to make the rise time more sensitive to increases in h, decreasing quicker. Eventually, however, the buoyancy will decrease enough due to the disappearing density contrast so as to once again stop diapirism.

Lastly, the existing coupling relationships are maintained while introducing a cap on grain size due to the effect of salt impurities pinning grain boundaries. This puts a limit on how large μ_L can grow, impacting the shape of the diapirs, as described in Section 2.2

$$R_L = 10^{(-6.896551724\times10^{-5})h} - 3.931034483 \quad (17)$$

The rise timescale of diapirs provides an important constraint on the role of salt diapirism in Europa's geological evolution. If diapir ascent occurs slowly relative to geological timescales, buoyant material may remain trapped within the ice shell for extended periods of time. Conversely, rapid diapir ascent would imply that compositional buoyancy can efficiently transport material through the ice shell, allowing diapirism to influence surface geology on shorter timescales.

Figures 6, 7, 8, and 9 show that across a range of parameters, **diapir rise occurs on geologically relevant timescales** of around $10^3 - 10^8$, spanning the convective overturn timescale of $10^4 - 10^5$ years (G. Mitri & A. P. Showman 2005). This supports previous studies that claim salt diapirism as a potential driver of the production of surface features such as domes and spots (lenticulae) (R. T. Pappalardo & A. C. Barr 2004). Figures 7 and 8 show that the **coupling of ρ_L and h works to place an upper limit on the size of diapirs, a conclusion that can be directly tied to observations of lenticulae size as well as how much material can be transfered in Europa's ice shell as a result of salt diapirism**. Figure 8 shows that coupling R_L and h makes $t_{\rm rise}$ more sensitive to h, with low viscosity diapirs forming from a thicker layer and rising faster. Eventually, the ρ_L coupling reverses the trend again, but now at a different maximum diapir size compared to the scenario where R_L and h are not coupled (Figure 7).

Future work will involve introducing further complexity into the model. This will include replacing the current linear coupling with more physically accurate coupling mechanisms based on empirical and laboratory studies. Additionally, we will consider how the viscosity contrast impacts the Stokes velocity calculation. These model enhancements will allow for quantitative predictions of maximum diapir size and material flux in Europa's ice shell.

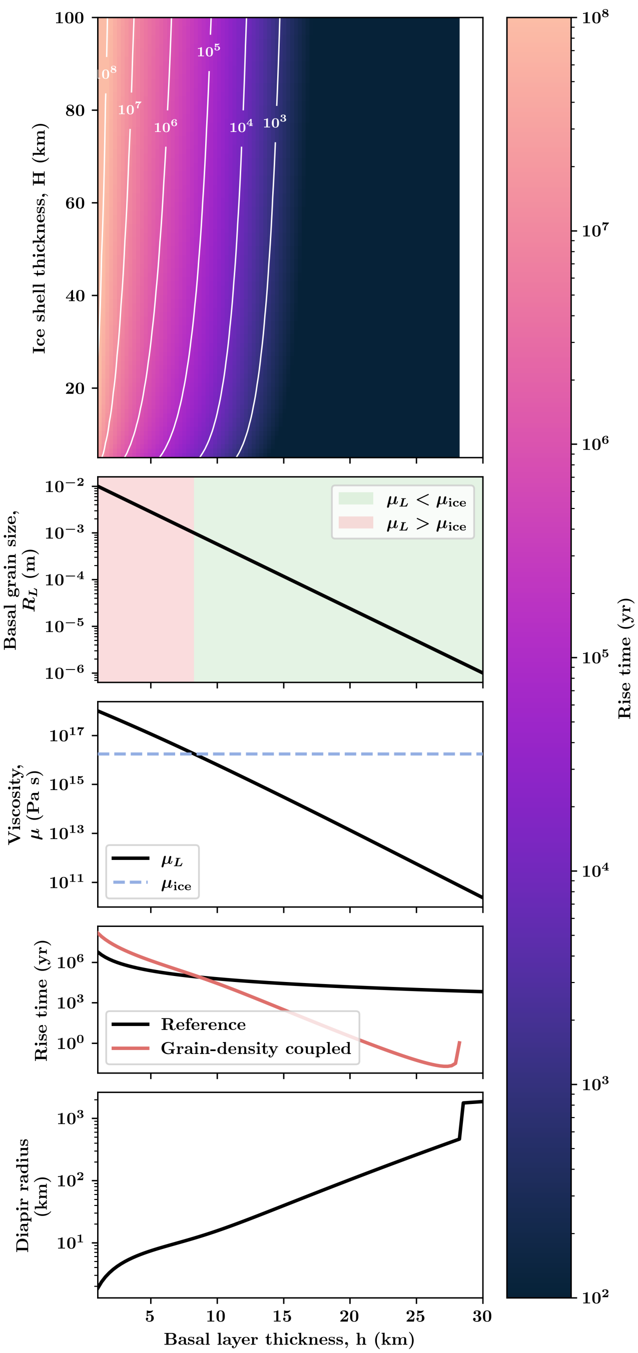

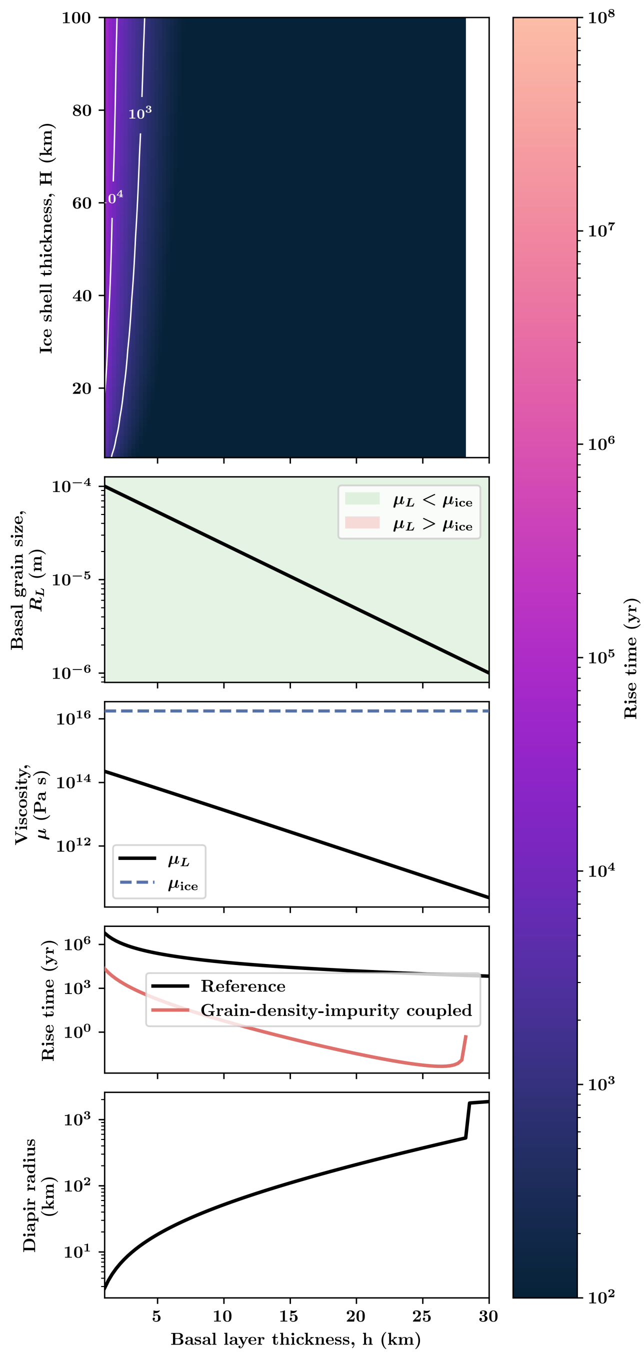

Figure 8. We introduce an additional coupling between R_L and h (Equation 16), where R_L decreases with h. The variation in R_L influences μ_L (Equations 11–12), an input in both the dominant wavelength used to determine diapir radius as well as v (Equation 7). The regime in which t_{rise} is larger or smaller than the reference depends on whether $\mu_L > \mu_{\mathrm{ice}}$. σ is kept constant for the sake of simplicity.

Figure 9. We implement an additional constraint on grain size due to salt impurities, which can cause pinning of grain boundaries (Equation 17). In this scenario, the switchm from $\mu_L < \mu_{\mathrm{ice}}$ to $\mu_L > \mu_{\mathrm{ice}}$ never occurs, and t_{rise} is reduced through the entire range of h as compared to the reference model run.

Table 2. Default parameter values used in model

Parameter	Definition	Value	Units
L	Horizontal length scale of modeled region	100	km
H	Ice shell thickness	40 or varied	km
dh/dt	Ice shell growth rate	2.5×10^{-11} or varied	m s^{-1}
P_{growth}	Timescale of ice shell growth	75	Ma
C_{ice}	Salt impurity concentration in ice shell	14.72	ppt
C_L	Salt impurity concentration in basal layer	1.053	ppt
ρ_{salt}	Density of entrained salt impurities	1300	kg m^{-3}
R_{ice}	Ice shell grain size	1	mm
R_L	Basal layer grain size	1 or varied	mm
σ	Shear stress	10^3	Pa
T_b	Basal temperature	243	K
T_s	Surface temperature	100	K
g	Surface gravitational acceleration	1.31	m s^{-2}
h	Basal layer thickness	Eq.9 or varied	m
ρ_{ice}	Ice shell density	Eq.14	kg m^{-3}
ρ_L	Basal layer density	Eq.14 or varied	kg m^{-3}
μ_{ice}	Effective viscosity of ice shell	Eqs.11–12	Pa s
μ_L	Effective viscosity of basal layer	Eqs.11–12 or varied	Pa s

Note— Parameters with given values are prescribed, while others are calculated through the listed equations. Parameters that are varied in certain runs of the model are stated to be so. Calculated quantities are determined internally from prescribed model parameters and the appropriate equations.

ACKNOWLEDGMENTS

Thank you to the CIERA REU program for providing the space and support for this project. This material is based upon work supported by the U.S. National Science Foundation (NSF) under Award Number AST-2446392. Any opinions, findings, and conclusions or recommendations expressed in this material are those of the author(s) and do not necessarily reflect the views of the NSF.

REFERENCES

Barr, A. C., & McKinnon, W. B. 2007, Journal of Geophysical Research: Planets, 112, doi: 10.1029/2006JE002781

Barr, A. C., & Pappalardo, R. T. 2005, Journal of Geophysical Research: Planets, 110, doi: 10.1029/2004JE002371

Barr, A. C., & Stillman, D. E. 2011, Geophysical Research Letters, 38, doi: 10.1029/2010GL046616

Buffo, J. J., Meyer, C. R., & Parkinson, J. R. G. 2021, Journal of Geophysical Research: Planets, 126, e2020JE006741, doi: 10.1029/2020JE006741

Buffo, J. J., Schmidt, B. E., Huber, C., & Walker, C. C. 2020, Journal of Geophysical Research: Planets, 125, e2020JE006394, doi: 10.1029/2020JE006394

Chandrasekhar, S. 1961, Hydrodynamic and hydromagnetic stability. https://ui.adsabs.harvard.edu/abs/1961hhs..book.....C

Chen, J.-C., Deschamps, F., & Hsieh, W.-P. 2026, Journal of Geophysical Research: Planets, 131, e2024JE008928, doi: 10.1029/2024JE008928

Deschamps, F., & Sotin, C. 2001, Journal of Geophysical Research: Planets, 106, 5107, doi: 10.1029/2000JE001253

Durham, W. B., Prieto-Ballesteros, O., Goldsby, D. L., & Kargel, J. S. 2010, Space Science Reviews, 153, 273, doi: 10.1007/s11214-009-9619-1

Hand, K. P., & Chyba, C. F. 2007, Icarus, 189, 424, doi: 10.1016/j.icarus.2007.02.002

Hussmann, H., & Spohn, T. 2004, Icarus, 171, 391, doi: 10.1016/j.icarus.2004.05.020

McKinnon, W. B. 1999, Geophysical Research Letters, 26, 951, doi: 10.1029/1999GL900125

Mitri, G., & Showman, A. P. 2005, Icarus, 177, 447, doi: 10.1016/j.icarus.2005.03.019

Nimmo, F., & Manga, M. 2009, Europa

Pappalardo, R. T., & Barr, A. C. 2004, Geophysical Research Letters, 31, doi: 10.1029/2003GL019202

Pappalardo, R. T., Head, J. W., Greeley, R., et al. 1998, Nature, 391, 365, doi: 10.1038/34862

Ren, Y., He, L., & Xia, H. 2024a, Journal of Polymer Science, 62, 3156, doi: 10.1002/pol.20230500

Roberts, J. H., McKinnon, W. B., Elder, C. M., et al. 2023, Space Science Reviews, 219, 46, doi: 10.1007/s11214-023-00990-y

Stoll, N., Eichler, J., Hörhold, M., Shigeyama, W., & Weikusat, I. 2021, Frontiers in Earth Science, 8, doi: 10.3389/feart.2020.615613

Tobie, G., Choblet, G., & Sotin, C. 2003, Journal of Geophysical Research: Planets, 108, doi: 10.1029/2003JE002099

Vance, S. D., Panning, M. P., Stähler, S., et al. 2018, Journal of Geophysical Research: Planets, 123, 180, doi: 10.1002/2017JE005341

Whitehead Jr., J. A., & Luther, D. S. 1975, Journal of Geophysical Research (1896-1977), 80, 705, doi: 10.1029/JB080i005p00705

Wolfenbarger, N. S., Fox-Powell, M. G., Buffo, J. J., Soderlund, K. M., & Blankenship, D. D. 2022, Journal of Geophysical Research: Planets, 127, e2022JE007305, doi: 10.1029/2022JE007305